Drag Balance for Hypervelocity Impulse Facilities

S. R. Sanderson* and J. M. Simmons†
University of Queensland, St. Lucia, Queensland 4072, Australia

A new technique is described for measuring drag with 100-μs rise time on a nonlifting model in a free piston shock tunnel. The technique involves interpretation of the stress waves propagating within the model and its support. A finite element representation and spectral methods are used to obtain a mean square optimal estimate of the time history of the aerodynamic loading. Thus, drag is measured instantaneously and the previous restriction caused by the mechanical time constant of balances is overcome. The effectiveness of the balance is demonstrated by measuring the drag on a cone with 15-deg semivertex angle in nominally Mach 5.6 flow with stagnation enthalpies from 2.6 to 33 MJ/kg. Measurement repeatability of about 10% is achieved.

Introduction

HYPERVELOCITY impulse facilities, such as free piston shock tunnels, have an important role in the development of technologies for hypersonic flight. They are capable of generating the high-enthalpy flows associated with external aerodynamics of space planes at near orbital velocities and the internal aerodynamics of scramjet propulsion systems. Important model test parameters are drag and thrust, but their measurement is complicated greatly by the very short test times of impulse facilities.

Bernstein[1] has produced a comprehensive review of the force measurement techniques used in short duration facilities during 1955–1970. With the decline of interest in hypersonic flight, few papers appeared after 1970. Bernstein outlines the two modeling assumptions that are inherent in force balances prior to the new techniques described here: the model behaves as a rigid body and the members of the force balance structure are simple, lumped parameter elements. Balances are then categorized as stiffness-dominated force balances or inertia-dominated accelerometer balances. As the time scale over which a force balance must operate is reduced, the stiffness of the balance members must be increased. Eventually, a situation is reached where the distributed mass and stiffness of the balance members are no longer insignificant. Tractions along the length of the balance structure elements are then no longer constant and accelerometers placed on the model do not accurately reflect its motion.

From the literature[1-8] we conclude that for practically sized models, stiffness-dominated balances are only suitable for test times $> \sim 200$ ms. Inertia-dominated accelerometer balances can lower this acceptable test time to only ~ 10 ms. None of the papers reviewed describe a technique that is appropriate for testing in the 1-ms flows experienced in free piston shock tunnels.

Aerodynamic force measurement in free piston shock tunnels is currently based on surface pressure measurements made at discrete pressure tappings on the surface of the model. Integration of the discretized pressure distribution to obtain drag is feasible only if model geometry is simple and if drag due to skin friction is insignificant. This paper describes a novel approach to direct measurement of drag, including skin friction, by interpreting the transient stress waves propagating within the model and its sting support. To date, shock tunnel models are restricted to configurations that generate negligible lift. The mechanical configuration of the drag balance is derived from the Hopkinson pressure bar[9] and modifications of it that have been used for dynamic testing of materials subjected to large transient stresses.[10,11]

Received May 23, 1990; revision received Oct. 18, 1990; accepted for publication Nov. 19, 1990.

*Graduate Student, Department of Mechanical Engineering; currently Graduate Student, Graduate Aeronautical Laboratories, California Institute of Technology, Pasadena, CA 91225.

†Professor and Dean, Faculty of Engineering. Member AIAA.

Mathematical Representations of a New Drag Balance

A new drag balance is shown diagrammatically in Fig. 1. The model, in this case, a cone at zero incidence and so subjected to drag only, is attached to a sting in the form of a slender cylindrical elastic bar. The sting is suspended by several vertical threads so that it is free to move in the axial (freestream) direction. The time history of drag applied to the model can be inferred from the output of strain gauges that respond to the passage of stress waves along the sting. The strain gauges are placed near the model end of the sting in order to maximize the observation time before the onset of complications caused by the return of stress waves reflected from the free (downstream) end of the sting. An axisymmetric mathematical representation of the elastic model, based on a finite element method, forms part of the drag measurement technique. Before describing this, we use the following two simple one-dimensional representations to provide, for use in model design, understanding of the behavior of shock tunnel models subjected to rapidly applied loads.

One-Dimensional Representation with Rigid Model

Consider a rigid model of mass m attached to a slender sting of cross-sectional area A_2. The sting is of such a length that stress waves reflected from its free end can be neglected on the time scale of concern. A simple approximation to the force applied to the model in a shock tunnel is a step force of magnitude P applied at time $t = 0$. Stress wave theory[12] gives Eq. (1) as the exponential response for the axial stress σ_x at the model (upstream) end of the sting:

$$\sigma_{x=0} = \rho_2 c_2 \frac{\partial u}{\partial t}\Big|_{x=0} = \frac{P}{A_2} \cdot [1 - e^{-t/\tau}] \tag{1}$$

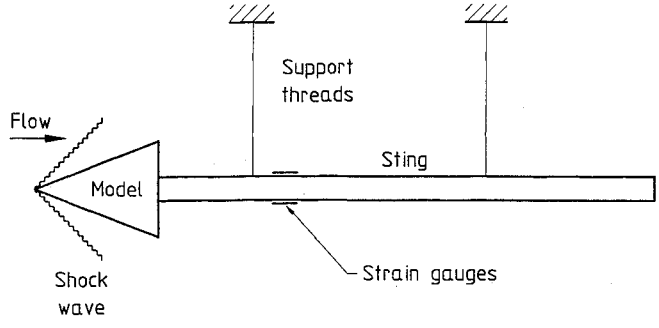

Fig. 1 Diagram of new drag balance.

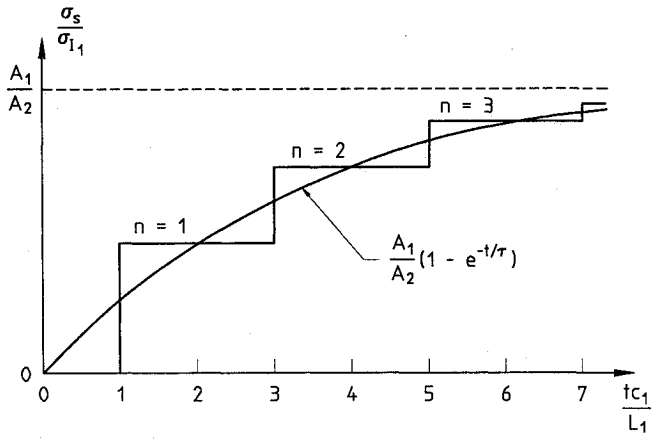

Fig. 2 Superposition of stress waves in sting immediately behind model in one-dimensional representation.

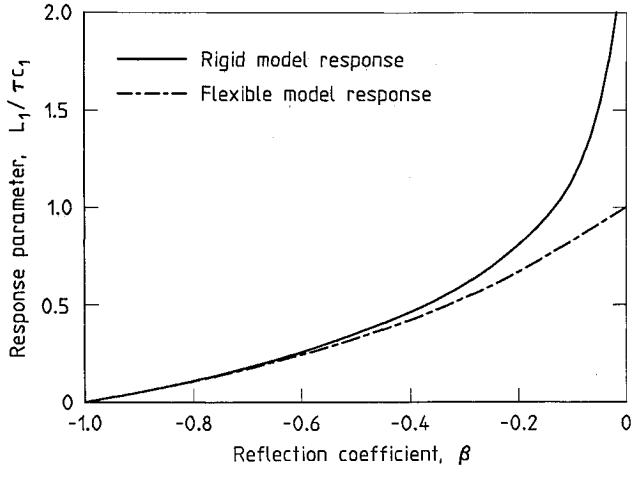

Fig. 3 Comparison of rigid and flexible one-dimensional model responses.

where ρ_2 is the density of sting material, c_2 the stress wave speed in sting, u the local sting displacement in x direction, and τ the balance time constant, $m/(\rho_2 c_2 A_2)$. The measured strain is proportional to this stress and asymptotically approaches the steady-state value. The model accelerates until the reaction exerted by the sting on the model asymptotically approaches the applied load. Then, the model approaches a constant velocity, with the applied aerodynamic load balanced by an inertia force associated with material in the sting being accelerated across the propagating stress wave.

One-Dimensional Representation with Elastic Model

Flexibility of the model is an important consideration in shock tunnel testing. Consider the conical model in Fig. 1 to be approximated by a uniform elastic cylinder of the same length L_1. The cross-sectional area of the cylinder A_1 is chosen so that the masses of the cone and cylinder are equal.

The cylinder is subjected to a step load P applied at $t = 0$ to its free end. This generates an incident compression stress wave of magnitude $\sigma_{I_1} = P/A_1$, which encounters the interface between the model and the sting. The result[12,13] is a transmitted wave of magnitude σ_{T_1} and a reflected wave of magnitude σ_{R_1}, where

$$\sigma_{T_1} = \alpha\sigma_{I_1} \tag{2}$$

$$\sigma_{R_1} = \beta\sigma_{I_1} \tag{3}$$

Transmission coefficient:

$$\alpha = \left[\frac{(2\rho_2 c_2)/(\rho_1 c_1)}{1 + (\rho_2 c_2 A_2)/(\rho_1 c_1 A_1)}\right] \tag{4}$$

Table 1 Reflection coefficients β, time constants τ, and test times T_2 from one-dimensional analysis of the prototype balance configuration with various material combinations

Model material	Sting material	β	τ, μs	T_2, ms
Nylon	Brass	− 0.080	102	1.1
Magnesium	Steel	− 0.632	171	0.8
Magnesium	Brass	− 0.706	226	1.1
Aluminum	Steel	− 0.746	268	0.8
Nylon	Aluminum	− 0.446	318	0.8
Aluminum	Brass	− 0.800	352	1.1
Steel	Steel	− 0.905	780	0.8
Aluminum	Aluminum	− 0.905	786	0.8
Brass	Brass	− 0.905	1112	1.1

Reflection coefficient:

$$\beta = \left[\frac{(\rho_2 c_2 A_2)/(\rho_1 c_1 A_1) - 1}{(\rho_2 c_2 A_2)/(\rho_1 c_1 A_1) + 1}\right] \tag{5}$$

where ρ_1 is the density of model material and c_1 is the stress wave speed in model. In practical configurations, β is negative so that σ_{R_1} is a tensile wave. The transmitted wave σ_{T_1} propagates along the infinitely long sting. The reflected wave is inverted when it reaches the free (upstream) end of the cylinder (model). It traverses the cylinder a second time and is again incident as a compression upon the interface. The magnitude of this second incident wave is

$$\sigma_{I_2} = \beta\xi\sigma_{I_1} \tag{6}$$

where $\xi = -1$ is the reflection coefficient for the free end of the cylinder.

The second incident wave yields at the interface

$$\sigma_{T_2} = \alpha\sigma_{I_2} = \alpha\beta\xi\sigma_{I_1} \tag{7}$$

$$\sigma_{R_2} = \beta^2\xi\sigma_{I_1} \tag{8}$$

Generally, after n incident waves at the interface,

$$\sigma_{T_n} = \alpha(\beta\xi)^{n-1}\sigma_{I_1} \tag{9}$$

$$\sigma_{R_n} = \beta(\beta\xi)^{n-1}\sigma_{I_1} \tag{10}$$

Consider the stress σ_s in the sting immediately behind the interface. After n waves have encountered this discontinuity,

$$\sigma_{s_n} = \sum_{j=1}^{n}\sigma_{T_j} = \sum_{j=1}^{n}\alpha(\beta\xi)^{j-1}\sigma_{I_1} = \alpha\sigma_{I_1}\sum_{j=1}^{n}(-\beta)^{j-1} \tag{11}$$

On each occasion that a stress wave encounters the interface, a successively smaller wave is transmitted along the sting (Fig. 2). From Eq. (11) as $n \to \infty$, it can be shown[13] that

$$\lim_{n\to\infty}\frac{\sigma_{s_n}}{\sigma_{I_1}} = \frac{\alpha}{1+\beta} = \frac{A_1}{A_2}; \qquad -1 < \beta < 1 \tag{12}$$

Thus, the limiting value of this series is the same as the steady-state stress level in the sting for applied load P.

Characterizing the Effect of Model Flexibility

A simple quantitative measure of the effects of model-sting geometry and materials can be obtained from a comparison of the step response for two cases: 1) when the model is treated as a rigid lumped mass, and 2) when the model is treated as elastic. We pass an exponential function of the form of Eq. (13) through the midpoints of the plateaus of Eq. (11) (Fig. 2):

$$\frac{\sigma_s}{\sigma_{I_1}} = \frac{A_1}{A_2}[1 - e^{-t/\tau}] \tag{13}$$

After n waves,

$$\frac{\sigma_{S_n}}{\sigma_{I_1}} = \frac{\alpha}{\alpha+\beta} - \alpha \sum_{j=n+1}^{\infty} (-\beta)^{j-1} = \frac{\alpha[1-(-\beta)^n]}{1+\beta} \tag{14}$$

Equating (13) and (14) and using $\alpha/(1+\beta) = A_1/A_2$ from Eq. (13), it follows that

$$n\ell n(-\beta) = -t/\tau; \qquad \beta<0 \tag{15}$$

Time t is related to n by the time taken for a stress wave to propagate from the interface to the free end of the cylinder (model) and back to the interface. Hence,

$$t = \frac{2L_1 n}{c_1} \tag{16}$$

Here, L_1 is the length of the model. The simple expression [Eq. (17)] then follows. It is a convenient means of investigating the performance of different model-sting configurations and materials during the design of a practical drag balance:

$$\tau = \frac{-2L_1}{c_1 \ell n(-\beta)} \tag{17}$$

This analysis is valid only for the interface reflection coefficient $\beta<0$, the impedance of the sting then being less than that of the model; i.e., $\rho_2 c_2 A_2 < \rho_1 c_1 A_1$. Choices of model and sting materials to give $\beta>0$ generally imply $A_2>A_1$, a configuration that is aerodynamically impractical.

The importance of model flexibility can be assessed by comparing the time constant $\tau = m/(\rho_2 c_2 A_2)$ for the rigid model with that given by Eq. (17) for the elastic model. Both are plotted in Fig. 3 in dimensionless form against interface reflection coefficient β. [Note that $m = \rho_1 L_1 A_1$, so that from Eq. (5) for the rigid model, $L_1/(\tau c_1) = (1+\beta)/(1-\beta)$.] For small values of β, model elasticity has considerable influence on the time constant of the drag balance. For a number of material combinations, Table 1 contains values of β, τ, from Eq. (17), and the test time $T_2 = 2L_2/c_2$, which is the time between passage of the initial stress wave into the sting and its return as a reflected wave from the free end of the sting. (Here, L_2 is the length of the sting and c_2 is the axial stress wave speed in it.) The values in Table 1 are based on the geometry of the prototype balance described later, viz., $A_1 = 3009$ mm^2, $A_2 = 154$ mm^2 and $L_2 = 2000$ mm.

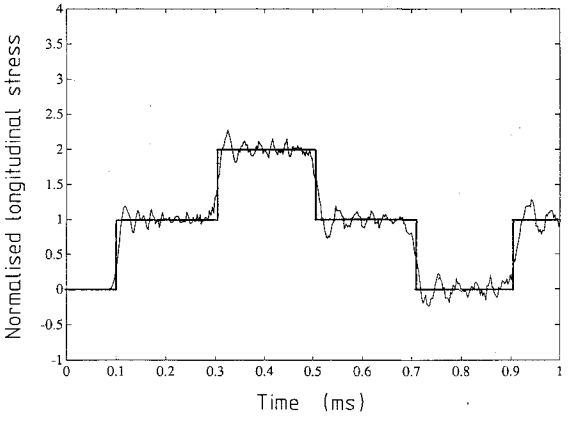

Fig. 4 Comparison of computed and analytical (straight lines) solutions for stress at midpoint of bar in uniform bar test case. Stress is normalized by static stress.

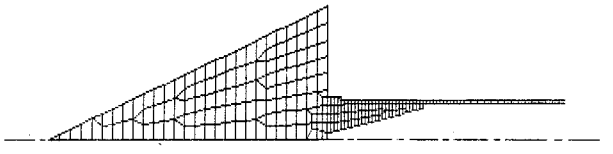

Fig. 5 Finite element mesh for cone and sting.

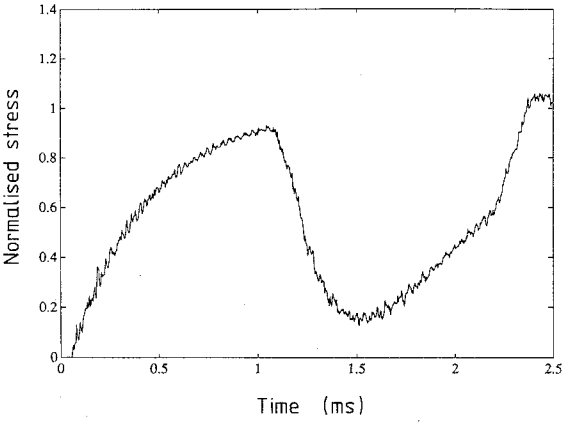

Fig. 6 Finite element solution (fine mesh) for stress at gauge location. Stress is normalized by static stress.

Table 1 indicates that the required small time constants are achieved with 1) light metal models and dense metal stings because stress waves traverse the model at high speeds, and 2) low impedance nylon models and any metallic sting through close impedance matching at the interface.

The selection of materials for the prototype drag balance is influenced by the response time as characterized by the time constant, the test time T_2, and noise levels. The signal-to-noise ratio from strain gauges can be increased by selecting a sting material with a low modulus of elasticity. Response time is arguably the most important parameter. Fabrication accuracy and engineering expedience favor bimetallic combinations. Of the less exotic combinations, an aluminium model and a brass sting represents the best compromise. The low damping in metals, compared with nylon, for example, is an advantage in terms of mathematical representation. It can be ignored without significant loss of accuracy.

Finite Element Representation

A more precise axisymmetric representation is needed for interpreting experimental data. This is achieved for a cone on a hollow cylindrical sting by spatial discretization with a finite element code based on that by Bathe.[14] The computational effort involved in the direct integration of the resulting second-order differential equations was minimized by using the Bulirsch-Stoer algorithm.[15]

Numerical Results

The finite element method was validated by computing the stress wave processes following the application of a step load to the free end of a free/fixed circular steel bar. The system was approximated by a mesh of axisymmetric bilinear quadrilateral elements. Axial stress at the midpoint of the bar, normalized with respect to the static stress, is shown in Fig. 4, with the one-dimensional analytical solution superimposed. Oscillations in the numerical solution arise from the coarseness of the mesh and non-one-dimensional wave propagation modes. The computed solution is seen to be valid after a considerable number of wave reflections.

The finite element method was next applied to the axisymmetric drag balance described in detail in the next section. The axisymmetric mesh is shown in Fig. 5. Except for a small stainless steel tip, the cone is constructed from aluminium. A tubular brass sting extends to a length of 2 m (not shown). The aerodynamic loading in time is modeled as a step uniform pressure acting on the surface of the cone, with base pressure assumed to be negligible. The output of the balance is the axial stress in the sting, as would be measured by strain gauges bonded to the surface of the brass tube 200 mm behind the base of the cone. Convergence of the numerical solution has

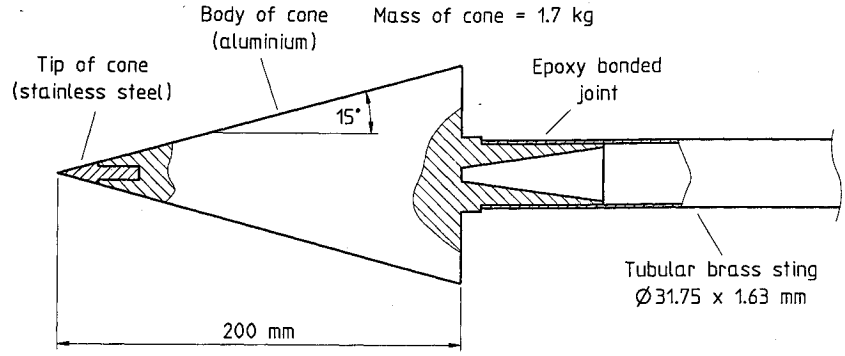

Fig. 7 Model-sting geometry for prototype balance.

been demonstrated[13] by changing the fineness of spatial and temporal discretization.

The solution is shown in Fig. 6. Oscillations are inevitable in a mathematical model that is analogous to an undamped array of masses and springs. The time constant determined from Fig. 6 is 420 μs, a value 20% higher than the 352 μs for the simple one-dimensional models that must be used only as design tools.

Effect of Load Distribution

For the operation of a static drag balance in the absence of lift, it is sufficient to make only one measurement to define the drag force. When the model cannot be treated as a rigid body, the output of the drag balance depends on both the magnitude of the drag and its distribution over the surface of the model. Conversely, from a single measurement, it is not possible to define uniquely the loading that produced the measured response. In reality, the loading distribution can be described adequately by a small number of parameters and, hence, by a small number of measurements. To avoid the need for a numerically accurate prediction of the stress waves propagating within the model, it is best to maximize the number of wave reflections within the model. These wave processes then need only be accurate in a general sense with any errors being averaged over a number of reflections. This results in a drag balance that is insensitive to loading distribution. Finite element computations[13] of the step responses, for both a uniform pressure distribution and a point load at the vertex of the cone, show no discernible sensitivity to load distribution for the proposed geometry.

Using the Computed Response to Obtain Drag

The dynamic behavior of a time-invariant, causal, linear system with single input $u(t)$ and single output $y(t)$ is described by the integral

$$y(t) = \int_0^t g(t-\tau)\, u(\tau)\, \mathrm{d}\tau \tag{18}$$

The preceding finite element analysis can be used to obtain the unit impulse response function $g(t)$ from the computed step response. In this section, the inverse dynamic problem is solved. A method is described for interpreting the noisy measured output to obtain the unknown aerodynamic drag $u(t)$ acting on the shock tunnel model.

For the discrete time problem, $u(t)$, $y(t)$, and $g(t)$ are replaced by the discrete time series u_i, y_i, and g_i; $i = 0, 1, 2,...$ The sampling interval is Δt and $t = i.\Delta t$. The convolution integral [Eq. (18)] becomes the summation,

$$y_i = \sum_{j=0}^{i} g_{i-j} \cdot u_j \tag{19}$$

Inverse dynamics problems are studied in many disciplines. Unfortunately, they are often poorly conditioned. Difficulties arise through the amplification of measurement noise by the inversion procedure.[16-19] The description of the problem is now expanded to include measurement noise $n(t)$ added to $y(t)$. In discrete time, the noise is n_i, the output of the system is y_i, and the measured output is $z_i = y_i + n_i$.

The inverse problem may be interpreted as a mean square estimation problem. We define the error function J as

$$J = \sum_{i=0}^{n-1} |u_i - \hat{u}_i|^2 \tag{20}$$

The real and estimated inputs to the system are $u_0, \ldots, u_{N-1}$ and $\hat{u}_0, \ldots, \hat{u}_{N-1}$, respectively, and N is the length of the data. Thus, the inverse problem comprises determining the estimator $\phi_0, \ldots, \phi_{N-1}$, where

$$\sum_{k=0}^{i} \phi_{i-k} z_k = \sum_{k=0}^{i} g_{i-k} \cdot \hat{u}_k; \qquad i = 0, 1,\ldots,N-1 \tag{21}$$

such that the expected value of the error function $\hat{J}$, given by Eq. (22), is minimized,

$$\hat{J} = E\left\{ \sum_{i=0}^{N-1} |u_i - \hat{u}_i|^2 \,|\, z_i; \qquad i = 0, 1,\ldots,N-1 \right\} \tag{22}$$

Here, $E\{\cdot\}$ denotes the expectation given the data z. We omit the reference to the data and, henceforth, all expectations may be taken as conditional on z.

Since each term of the summation is ≥ 0, an equivalent requirement for an optimal estimate is that

$$\hat{J}_i = E\{|u_i - \hat{u}_i|^2\} \tag{23}$$

be minimum for $i = 0,\ldots, N-1$. Generally, mean square estimation problems such as this may be solved by application of the orthogonality principle.[20] For $\hat{J}_i$ to be a minimum we require that

$$E\{(u_i - \hat{u}_i)\bar{z}_i\} = 0; \qquad i = 0,1,\ldots,N-1 \tag{24}$$

That is, the estimation error $(u_i - \hat{u}_i)$ is orthogonal to the data z_i. Note that we must reconstruct the aerodynamic load before its effect is sensed by the strain gauges. This is apparent from consideration of the implicit form of Eq. (21) for $\hat{u}$. Hence, we must implement an acausal algorithm to solve the inversion problem and consequently we define the error function J for both future and past times. The noncausal nature of the inversion problem precludes the use of the more common Weiner-Hopf and Kalman[20] prediction and filtering results. Whereas these techniques may be applied to the acausal smoothing problem, the implicit nature of the right side of Eq. (21) distinguishes the smoothing and inversion problems. Press et al.[15] note that an elegant solution to the inversion problem may be obtained using spectral methods and they derive the result in a deterministic manner. Continuing with the current stochastic formulation we note that Parseval's

identity may be used to define the error function in the frequency domain,

$$\hat{J} = E\left\{\sum_{j=0}^{N-1} |U_j - \hat{U}_j|^2\right\} \tag{25}$$

Equivalently,

$$\hat{J}_j = E\{|U_j - \hat{U}_j|^2\}; \qquad j = 0, 1,\ldots,N-1 \tag{26}$$

and for an optimal estimate, Eq. (24) implies,

$$E\{(U_j - \hat{U}_j)\bar{Z}_j\} = 0; \qquad j = 0, 1,\ldots,N-1 \tag{27}$$

Using the convolution property of the Fourier transform, we write Eq. (21) as,

$$\hat{U}_j = \frac{\Phi_j Z_j}{G_j}; \qquad j = 0, 1,\ldots,N-1 \tag{28}$$

Substituting for $\hat{U}_j$ in Eq. (27) gives,

$$E\left\{\left(U_j - \frac{\Phi_j Z_j}{G_j}\right)\bar{Z}_j\right\} = 0; \qquad j = 0, 1,\ldots,N-1 \tag{29}$$

Note the intractability of the substitution in the time domain. Since $Y_j = G_j U_j$,

$$E\left\{\frac{Y_j \bar{Z}_j}{G_j} - \frac{\Phi_j Z_j \bar{Z}_j}{G_j}\right\} = 0; \qquad j = 0, 1,\ldots,N-1 \tag{30}$$

For $G_j \neq 0$, this implies that

$$E\{(Z_j - N_j)\bar{Z}_j - \Phi_j Z_j \bar{Z}_j\} = 0$$

where N_j represents the measurement noise. It follows that

$$E\{Z_j \bar{Z}_j(1 - \Phi_j) - N_j(\bar{Y}_j + \bar{N}_j)\} = 0$$

Since n_i and y_i are uncorrelated,

$$(1 - \Phi_j)E\{Z_j \bar{Z}_j\} - E\{N_j \bar{N}_j\} = 0; \quad j = 0, 1,\ldots,N-1 \tag{31a}$$

$$\Phi_j = \frac{S_{zz,j} - \nu_j}{S_{zz,j}}; \qquad j = 0, 1,\ldots,N-1 \tag{31b}$$

Thus, given the power spectral density of the data S_{zz} and the noise variance ν as a design parameter, Eq. (31) determines the optimum filter Φ. Combining the filter with the impulse response function in Eq. (28), we obtain the mean square optimal solution of the inverse problem,

$$\hat{u}_i = F^{-1}\left[\frac{\Phi_j Z_j}{G_j}\right]; \qquad i,j = 0, 1,\ldots,N-1 \tag{32}$$

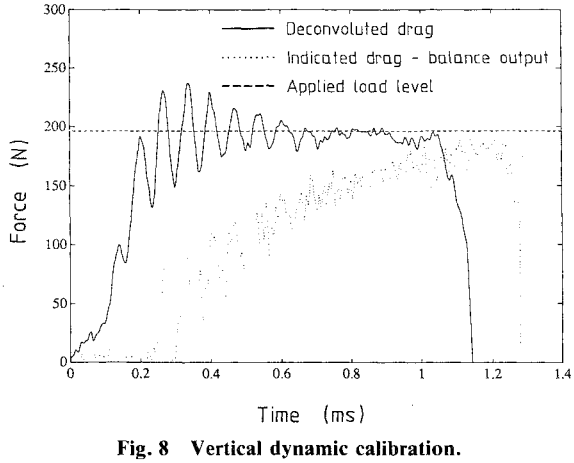

Fig. 8 Vertical dynamic calibration.

Here F^{-1} denotes the inverse discrete Fourier transform to be evaluated using standard fast Fourier transform (FFT) algorithms.[15]

A further consequence of the use of discrete Fourier transforms is the implicit assumption of N periodicity of the signals. This conflicts with the causal nature of the physical system as defined by Eq. (18). By padding all time series to twice their length with trailing zeros, causality is enforced for the first half of the signal.[15] Subsequent application of the discrete Fourier transform provides the desired acausal filter properties.

Implementation of a Drag Balance

This section contains a description of experiments conducted to evaluate a prototype drag balance in the University of Queensland T4 free piston shock tunnel.

Model and Sting

The model-sting geometry is shown in Fig. 7. The 15-deg semivertex angle results in a weak bow shock wave behind which the composition of the nitrogen test gas can be assumed to be frozen at the composition existing at the exit of the shock tunnel nozzle. The ratio of surface area to frontal area is low so that skin friction is only a minor component of the total drag. The mass of the cone is 1.7 kg.

The sting was constructed from hollow tubing to make its bending stiffness high relative to its axial stiffness, thereby simplifying the supporting of it in the test section to minimize non-one-dimensional effects. For consistency with the finite element representation, a continuous contact surface between the model and the sting was achieved with an epoxy adhesive. The sting was suspended horizontally in the test section with two vertical wires. This provides vibration isolation in the horizontal plane. Bending effects from tunnel vibration excitation in the vertical direction are canceled by using two diametrically opposed foil resistance strain gauges cemented to the sting 200 mm from the base of the cone. To shield the sting from the flow, the sting and the supporting wires were enclosed in a close fitting shroud. The freely suspended model could not reach significant velocity during the 1-ms duration of the test flow.

Data Acquisition

The outputs of the drag balance and the general shock tunnel instrumentation were recorded on an 11-bit digital event recorder, each channel of which recorded 2048 samples with a sampling time of 5 μs.

Obtaining the Impulse Response

The unit impulse response function was obtained from the finite element computation by differentiation of the step response of the balance. The computed step response in Fig. 6 exhibits nonphysically significant oscillations associated with the spatial discretization of the governing equations. To avoid differentiating these oscillations a ninth-order polynomial is first fitted to the computed step response. The discretized impulse response is scaled to represent the response of the balance to a load of 1 N applied for 5 μs (one sampling interval).

Experimental Results

Dynamic Calibration of Balance

The drag balance was calibrated dynamically to validate the deconvolution procedure. A known weight was suspended from the vertex of the cone by a highly stressed steel wire, which, when cut, provided a rapid step unloading of the model. This process was performed with the model and sting suspended both vertically from the free end of the sting and horizontally in the test section of the shock tunnel. The vertical test was considered to be the more accurate, but the horizontal test was needed to show that the sting suspension sys-

tem in the test section has an insignificant effect on the performance of the balance.[13] The raw balance output from a vertical test with a statically calibrated strain gauge bridge, the drag history deconvoluted from it, and the level of applied loading are compared in Fig. 8. The computed drag measurement is a valid estimate of the applied load until the arrival of the stress wave reflected from the rear end of the sting.

Drag Measurements in Shock Tunnel

Nitrogen was used as the test gas in the T4 shock tunnel to minimize chemical reactions, thereby simplifying comparison of drag measurements with theory. Eight test section stagnation enthalpies were used, from 2.6 to 33 MJ/kg. The test section conditions were computed from measurements of primary shock speed, test section pitot pressure, shock tube filling pressure, and nozzle stagnation pressure after primary shock reflection.

Figures 9 and 10 show two representative results. Each comprises plots of force balance output, test section pitot and nozzle stagnation pressure histories, and the ratio of test section pitot pressure to stagnation pressure, allowing for the flow transport time through the nozzle. Also plotted is the prediction of cone drag from the inviscid Taylor-Maccoll[21] theory for a perfect gas (frozen chemistry) attached conical shock and no base pressure.

The test section conditions in the captions of Figs. 9 and 10 correspond to conditions that existed at the start of steady flow in the test section, as determined from the constant ratio of pitot pressure to stagnation pressure. The start of the line for predicted drag marks the beginning of steady flow and

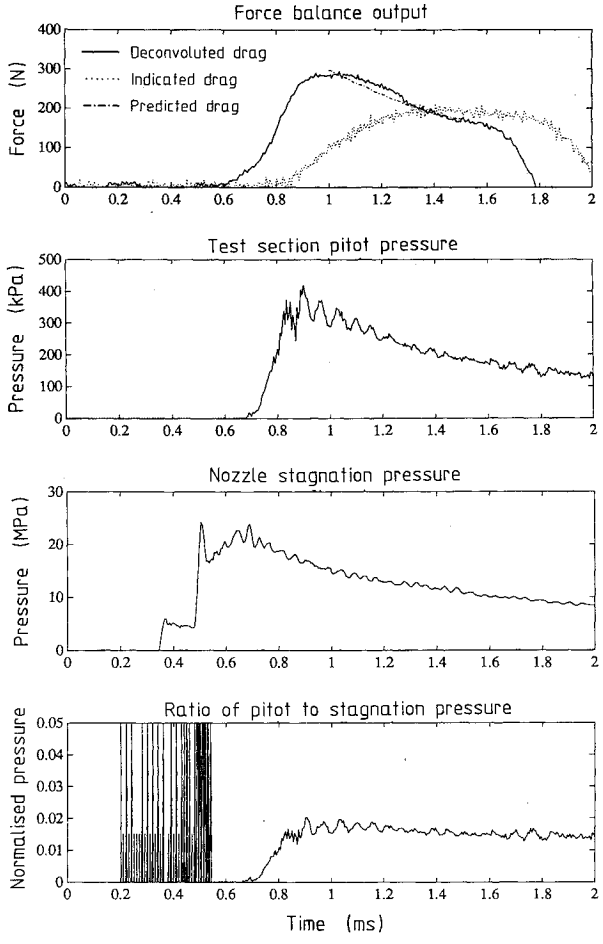

Fig. 9 Experimental results for nozzle stagnation enthalpy of 3.96 MJ/kg: Mach number = 6.9; velocity = 2640 m/s; static pressure = 6.64 kPa; pitot pressure = 320 kPa; static temperature = 450 K; density = 0.0492 kg/m^3; γ = 1.40.

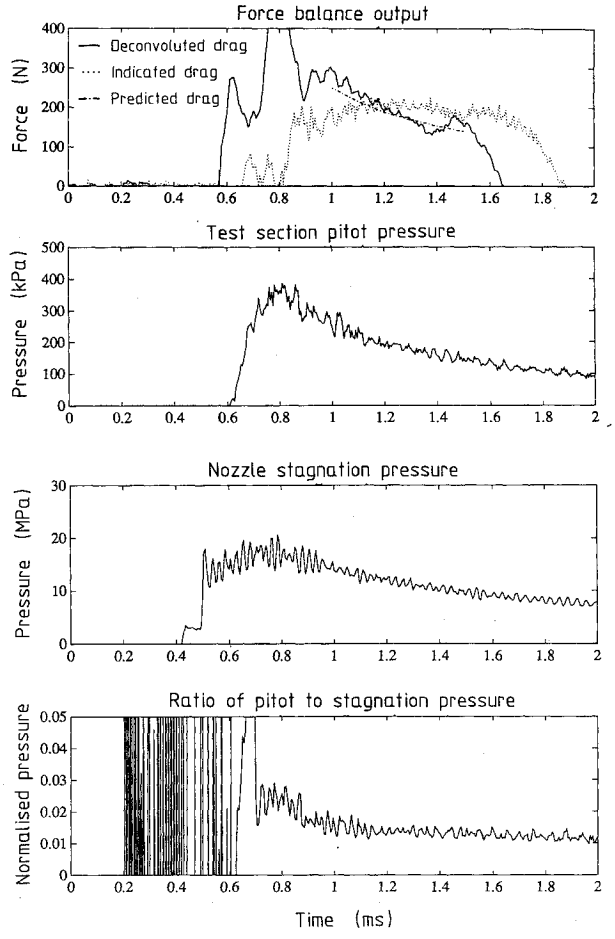

Fig. 10 Experimental results for nozzle stagnation enthalpy of 17.2 MJ/kg: Mach number = 5.4; velocity = 5000 m/s; static pressure = 6.86 kPa; pitot pressure = 256 kPa; static temperature = 2090 K, density = 0.0105 kg/m^3; γ = 1.32.

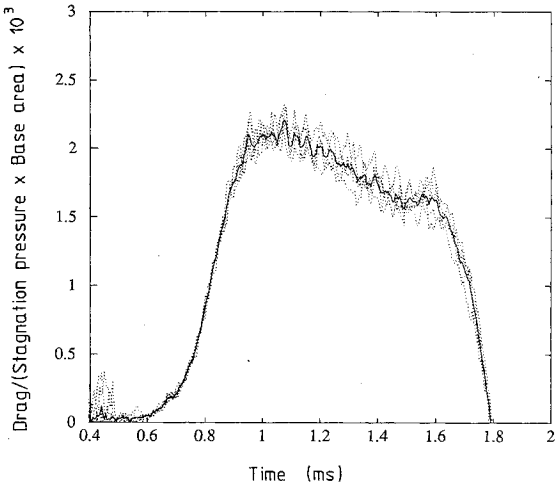

Fig. 11 Comparison of deconvoluted drag histories from repeated tests at conditions nominally identical to those defined in the caption to Fig. 9: superimposed dotted lines are for five tests; solid line is the average of five tests.

shows the predicted drag for the computed test section conditions. The predicted drag at other times is obtained by scaling the test section conditions according to the measured instantaneous pitot pressure. The oscillations at the beginning of the normalized pressure trace are due to division by zero and have no physical significance.

Figures 9 indicate that the deconvoluted drag follows the test section pitot pressure after about 100 μs from the peak of the pitot pressure. Because of its 400-μs mechanical time con-

stant, the uncompensated balance is not able to follow the fast initial development of the flow over the model, but it is sufficiently fast to follow the flow during the period of steady flow. Later, the uncompensated balance overshoots due to the delay in transmission of the unloading wave as the tunnel stagnation pressure falls. The deconvoluted drag measurement follows the pitot pressure until the arrival of the stress wave reflected from the free end of the sting.

Accuracy

The repeatability of the technique was assessed by comparing deconvoluted drag histories for multiple shock-tunnel tests at the same nominal conditions. This does not account for any systematic error due to inaccuracy of the finite element model. However, the accuracy of this model was confirmed by the dynamic calibration (Fig. 8). Figure 11 compares the deconvoluted drag histories from five tests at the conditions in the caption for Figs. 9. To eliminate the effect of slight variations in test conditions for each test, the drag data has been normalized by the instantaneous stagnation pressure and the cone base area. On the basis of these results, the technique is conservatively estimated to give results repeatable to $\pm 10\%$ under the operating conditions used.

Conclusions

A prototype drag balance has been developed and its use demonstrated in a free piston shock tunnel. The time history of the drag applied to the model is inferred from the output of strain gauges that respond to the passage of stress waves along the sting. Preliminary tests indicate that drag measurements agree with predictions for a model on which drag due to skin friction is small. The uncertainties of about 10% are acceptable, considering the penalty imposed by the short test time and the harsh operating environment.

Simple one-dimensional representations of the model-sting system are useful in designing practical balances. However, a finite element representation is needed to obtain an accurate impulse response function for the deconvolution procedure. For situations in which the drag is not dependent significantly on the loading distribution, impulse response functions might be obtained from the dynamic calibration procedure described earlier, but care would be needed to ensure sufficiently fast removal of the load. A finite element method will be required for design of balances when model geometry is too complicated to permit useful results from one-dimensional representations.

The use of nonmetallic materials such as nylon is worth investigation because much shorter response times can then be obtained. However, the effects of material damping would need careful consideration. In principle, the basic technique of the balance is extendable to measurement of drag in the presence of lift and to simultaneous measurement of lift, drag, and moments.

Acknowledgments

This study was supported by Australian Research Council Grant A4 851508P. The authors are grateful for suggestions from R. J. Stalker of the Department of Mechanical Engineering, the University of Queensland, St. Lucia, Queensland, Australia.

References

[1]Bernstein, L., "Force Measurement in Short-Duration Hypersonic Facilities," Dept. of Aeronautical Engineering, Queen Mary College, University of London, AGARDograph 214, 1975.

[2]Ledford, R. L., Smotherman, W. E., and Kidd, C. T., "Recent Developments in Heat-Transfer-Rate, Pressure and Force Measurements for Hot-Shot Tunnels," *IEEE Transactions on Aerospace and Electronic Systems,* Vol. AES-4, No. 2, 1968, pp. 202–209.

[3]Beaussier, J., "A Six-Component Balance," *IEEE Transactions on Aerospace and Electronic Systems,* Vol. AES-4, No. 2, 1968, pp. 210–217.

[4]Duryea, G. R., and Martin, J. F., "An Improved Piezo-Electric Balance for Aerodynamic Measurements," *IEEE Transactions on Aerospace and Electronic Systems,* Vol. AES-4, No. 3, 1968, pp. 351–359.

[5]Kussoy, M. I., and Horstmann, C. C., "Cone Drag in Rarefied Hypersonic Flow," *AIAA Journal,* Vol. 8, No. 2, 1970, pp. 315–320.

[6]Duryea, G. R., and Sheeran, W. J., "Accelerometer Force Balance Techniques," *IEEE Transactions on Aerospace and Electronic Systems,* Vol. AES-5, No. 4b, 1969, p. 688.

[7]Reddy, N. M., "Aerodynamic Force Measurements in the IISc Hypersonic Shock Tunnel," *Proceedings of the 14th International Symposium on Shock Tubes and Waves,* edited by R. D. Archer and B. E. Milton, New South Wales Univ. Press, Sydney, Australia, 1985, pp. 358–362.

[8]Bernstein, L., and Stott, G. T., "A Laser-Interferometric Trajectory-Following System for Determining Forces on Freely Flying Models in a Shock-Tunnel," *Proceedings of the 13th International Symposium on Shock Tubes and Waves,* edited by C. E. Treanor and J. G. Hall, State Univ. of New York Press, Albany, NY, 1981.

[9]Hopkinson, B., "A Method of Measuring the Pressure Produced in the Detonation of High Explosives and by the Impact of Bullets," *Philosophical Transactions of the Royal Society of London, Series A,* Vol. 213, Jan. 1914, pp. 437–456.

[10]Kolsky, H., "An Investigation of the Mechanical Properties of Materials at Very High rates of Loading," *Proceedings of the Physical Society, Section B,* Vol. 62, Pt. 11, 1949, pp. 676–700.

[11]Lindholm, U. S., "High Strain Rate Tests," *Techniques of Materials Research,* Vol. 5, Pt. 1, edited by R. F. Bunshah, Interscience, New York, 1971.

[12]Kolsky, H., *Stress Waves in Solids,* Dover, New York, 1963.

[13]Sanderson, S. R., "Drag Measurement Techniques for Short Flow Duration Hypervelocity Shock Tunnels," M.Eng.Sc. Thesis, Dept. of Mechanical Engineering, Univ. of Queensland, Queensland, Australia, 1989.

[14]Bathe, K. T., *Finite Element Procedures in Engineering Analysis,* Prentice-Hall, Englewood Cliffs, NJ, 1982.

[15]Press, W. H., Flannery, B. P., Teukolsky, S. A., and Vetterling, W. T., *Numerical Recipies: The Art of Scientific Computing,* Cambridge Univ. Press, London, UK, 1986.

[16]Goodier, J. N., Jahsman, W. E., and Ripperger, E. A., "An Experimental Surface-Wave Method for Recording Force-Time Curves in Elastic Impacts," *Journal of Applied Mechanics,* Vol. 26, March 1959, pp. 3–7.

[17]Stump, B. W., and Johnson, L. R., "The Determination of Source Properties by the Linear Inversion of Seismograms," *Bulletin of the Seismological Society of America,* Vol. 67, No. 6, 1977, pp. 1489–1502.

[18]Michaels, J. E., and Pao, Y. H., "The Inverse Source Problem for an Oblique Force on an Elastic Plate," *Journal of the Acoustical Society of America,* Vol. 77, No. 6, 1985, pp. 2005–2011.

[19]Robinson, E. A., *Multichannel Time Series Analysis with Digital Computer Programs,* Holden-Day, San Francisco, CA, 1967.

[20]Papoulis, A., *Probability, Random Variables and Stochastic Processes,* McGraw-Hill, New York, 1984.

[21]Taylor, G. I., and Maccoll, J. W., "The Air Pressure on a Cone Moving at High Speed," *Proceedings of The Royal Society of London, Series A,* Vol. 139, 1932, pp. 278–297.